

GROWTH AND CHARACTERIZATION OF ZIRCONIUM TELLURIDE ZRTE₅

A Thesis

in Partial Fulfilment of the Requirements for the

Degree of Master of Science

with a

Major in Physics

in the

College of Graduate Studies

University of Idaho

by

Ashwaq Alanazi

Major Professor: David N. McIlroy, PhD.

Committee Members: Leah Bergman, PhD., Matthew M. Hedman, Ph.D.

Department Administrator: Ray Von Wandruszka, Ph.D.

May 2018

Authorization to Submit Thesis

The thesis of Ashwaq Fahad Alanazi, submitted for the degree of Master of Science with a Major in Physics and titled, " GROWTH AND CHARACTERIZATION OF ZIRCONIUM TELLURIDE ZRTE₅," has been reviewed in final form. Permission, as indicated by the signatures and dates given below, is now granted to submit final copies to the College of Graduate Studies for approval.

Major Professor: _____ Date: _____

David N. McIlroy, Ph.D.

Committee Members: _____ Date: _____

Leah Bergman, Ph.D.

_____ Date: _____

Matthew M. Hedman, Ph.D.

Department Administrator: _____ Date: _____

Ray Von Wandruszka, Ph.D.

Abstract

Transition metal Pentatelluride ZrTe_5 is a versatile material in condensed-matter physics and has been widely studied since the 1980s. ZrTe_5 crystallizes in the orthorhombic layered structure that held together with space group Cmcm . The motivation of this study was to grow and characterize ZrTe_5 . So, by means of chemical transport reaction, the crystals of ZrTe_5 were successfully grown by using iodine (I_2) as a transport agent. Samples were prepared in different concentrations to grow successful ZrTe_5 . The samples were characterized by using X-ray diffraction (XRD) to identify the crystal phase, X-ray photoemission spectroscopy (XPS) to determine the binding energy, and scanning electron microscopy (SEM) to investigate the shape of ZrTe_5 .

Keywords:

Crystal ZrTe_5 growth; Chemical vapor transport; Crystal structure; Topological material

Acknowledgments

I would like to thank all those who made this research possible. First and foremost, I extremely would like to thank Professor David N. McIlroy for his unwavering guidance and insight throughout the supervision process. Besides that, I offer sincere gratitude to Dr. Leah Bergman, and Dr. Matthew M. Hedman for being my committee members and for their invaluable feedback and help. I also take this opportunity to express a deep sense of gratitude to Thomas Williams for his assistance. A great thanks to Aaron Babion and Negar Rajabi for their assistance during the period of my project work. Last but not least, thanks for my supportive and loving family, especially my parents and certainly my husband for his support and assist while I was working on this project.

Dedication

This thesis is dedicated to my parents who educated and enabled me to reach at this level, my husband and my sons who supported and encouraged me with strong love, my supportive siblings, especially my lovely sister who taught me to believe in myself, and my beloved friends for the inspiration that they gave me along the way.

Table of Contents

Authorization to Submit Thesis	ii
Abstract.....	iii
Acknowledgements.....	iv
Dedication.....	v
Table of Contents	vi
List of Figures	viii
List of Tables.....	ix
CHAPTER 1: Introduction.....	1
1.1. Structural and Topological Properties of ZrTe ₅	2
1.1.1. Crystal Structure	2
1.1.2. Transport Properties of Zirconium Telluride (ZrTe ₅).....	4
1.1.2.1. Resistivity	4
1.1.2.2. Thermopower.....	5
1.1.2.3. Positive Magnetoresistance	5
1.1.3. Topological Properties of ZrTe ₅	5
1.1.4. Topological Insulators.....	6
1.2. Applications of Zirconium Telluride.....	7
1.3. Potential Applications as Double Layered Thermoelectrics	9
CHAPTER 2: Experimental Materials.....	10
2.1. Raw Materials	10
2.2. Crystal Growth	10
2.3. Growth Mechanism.....	10

2.4. The Usage of Nitrogen	12
2.5. Calculations for Producing $ZrTe_5$	12
CHAPTER 3: Experimental Technique.....	14
3.1. Crystal Characterization	14
3.1.1. X-Ray Diffraction (XRD)	14
3.1.1.1. Powder X-Ray Diffraction	15
3.1.1.2. Single Crystal X-Ray Diffraction.....	16
3.1.2. X-Ray Photoelectron Spectroscopy	18
3.1.3. Scanning Electron Microscope.....	19
CHAPTER 4: Results	20
4.1. X-Ray diffraction Results.....	20
4.2. X-Ray Photoelectron Spectroscopy (XPS) Results.....	23
4.3. Scanning Electron Microscope (SEM) Results	27
CHAPTER 5: Discussion	32
5.1. Procedure of the Crystal Growth.....	32
5.2. X-Ray Diffraction.....	33
5.3. X-Ray Photoelectron Spectroscopy.....	35
5.4. Scanning Electron Microscope.....	37
CHAPTER 6: Conclusions.....	39
References.....	40
Appendix.....	47

List of Figures

Figure 1.1 The schematics of ZrTe ₅ crystal structure along a-, b- and c- direction.....	2
Figure 2.1 (a) schematic shows the CVT growth furnace of ZrTe ₅ single crystal. (b) Picture of the grew up of ZrTe ₅ single crystals on the internal surface of the tube.....	11
Figure 3.1 shows the sample inside SEM instrument.....	19
Figure 4.1 X-Ray diffraction patterns of (a) first attempt, (b) sixth attempt, (c) fifth attempt, and (d) fourth attempt respectively	20
Figure 4.2 Was Taken from (Lv et al, 252) as a reference	21
Figure 4.3 X-Ray diffraction pattern of the last attempt.....	22
Figure 4.4 XPS survey spectra of the sample with Zr = 0.0675 and Te = 0.469 for the binding energy range between 0 – 700 eV	23
Figure 4.5 The high-resolution XPS of the Zr 3d and the characteristic 3d _{3/2} and 3d _{5/2} doublet of Zr and Te of the first sample	24
Figure 4.6 XPS survey spectra of the sample 2 with Zr = 0.05 and Te = 0.361 for the binding energy range between 0 – 700 eV, and characteristic peaks of Zr, Te	25
Figure 4.7 The high-resolution XPS of the Zr 3d and the characteristic 3d _{3/2} and 3d _{5/2} doublet of Zr and Te of the second sample.....	26
Figure 4.8 X-ray photoemission spectroscopy (XPS) results of binding energies of Zr and Te	26
Figure 4.9 The first attempt of growing nanosprings on a chip of silica.....	27

Figure 4.10 An SEM image for the sixth sample and of coating ZrTe ₅	28
Figure 4.11 The layers of ZrTe ₅ for the sixth sample in different magnifications	29
Figure 4.12 The fourth attempt of growing ZrTe ₅ when the concentration of Zr: Te is 2 g.20	
Figure 4.13 The last attempt of growing ZrTe ₅ when the concentration of the transport agent increased to 1.2 g while the mixture of Zr; Te was 1 g	31

List of Tables

Table 2.1: Calculations for Producing ZrTe ₅	13
Appendix: General Information about Zirconium and Tellurium	47

CHAPTER 1: Introduction

Pentatelluride materials, such as ZrTe_5 , have been studied widely from the first time they were synthesized back in 1973 [1]. The reason starts from the interesting transport properties that these materials possess, especially with respect to the resistivity peak at a characteristic temperature, T^* , which is about 60K [2], and a sudden switch of the sign of the thermos-power at the same T^* [3].

ZrTe_5 belongs to a category of layered transition metal tellurides with a general formula MTe_n , where M is a transition metal with $n = 1, 2, 3, \text{ or } 5$ [31]. MTe_n represents many compounds by combination of the elements (M) and stoichiometry (n) [65]. A few materials from this family have also been studied widely because of their interesting physical properties. For instance, WTe_2 has gained a lot of popularity because of its non-immersing giant magnetoresistance [4] and, with MoTe_2 [5], has additionally been anticipated to be a type II Weyl semimetal [6], another category of quantum matter. Moreover, ZrTe_5 has been hypothetically predicted to have a place with another group of topologically non-trivial materials, i.e. a triple-point topological metals [7]. In the last years, an extreme argument about its topological character has been developed. However, an unclear experimental verification of the topological character of ZrTe_5 is still elusive [31].

The motivation of this thesis is to prove the growth of ZrTe_5 by means chemical vapor transport (CVT) and characterize it by several systems.

1.1 Structural and Topological Properties of ZrTe_5

1.1.1 Crystal Structure

ZrTe_5 is a material that crystallize in the orthorhombic layered crystal structure with space group Cmcm . Along the a-axis, the crystal structure is shaped as a result of trigonal prismatic chains of ZrTe_3 [31]. The prismatic chains are linked along the c axis by zigzag chains of Te atoms to form two-dimensional (2D) ZrTe_5 layers in the a – c plane. The layers of ZrTe_5 stack along the b-axis making a layered structure [31]. The primitive unit cell contains two formula units with two prismatic chains and two zigzag chains [31].

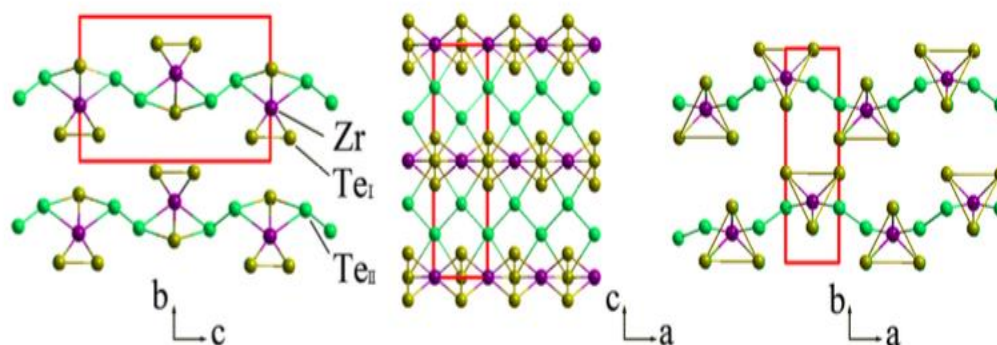


Figure 1.1 The schematics of ZrTe_5 crystal structure along a-, b- and c- direction projections. The red rectangles highlight the unit cell of ZrTe_5 . TeI and TeII represent the Te atom in the ZrTe_3 trigonal prismatic and inter-chain site, respectively [51].

ZrTe₅ crystals are orthorhombic and analytical techniques such as convergent beam diffraction showed that in certain cases, these crystals did not possess any diffraction zone axes, which is expected from mmm point group material system. It is even suggested that ZrTe₅ could be a polymorph system, i.e. a crystal that can exist in more than one crystal structure [55]. It is also reported that in the absence of higher axes of symmetry, this material could take up a monoclinic crystal point group, the unit cell parameters corresponding to its monoclinic form as $a_m = 4.12 \text{ \AA}$, $b_m = 13.7 \text{ \AA}$, $c_m = 7.5 \text{ \AA}$ and $\beta = 111^\circ$. However, in its orthorhombic form, the crystal parameters are $a_o = 3.97 \text{ \AA}$, $b_o = 14.502 \text{ \AA}$, $c_o = 13.726 \text{ \AA}$, and $\alpha = \beta = \gamma = 90^\circ$, showing its different crystallographic parameters in its two distinct forms [56].

The crystallographic information such as the reflection planes, the space groups, the parameters at different reflection axes, etc. have been studied and solved for the orthorhombic and the monoclinic structures of ZrTe₅ and has been quite effectively summarized by Sambongi et al in their paper [56]. These crystallographic parameters were solved from different X-ray diffraction photographs and other analytical techniques [56]. In certain instances, the variations in electrical resistivity was also assigned to the monoclinic/orthorhombic nature of the material. Temperature based X-Ray diffraction studies also showed phase transformations taking place at low temperatures which resulted in its interesting electrical properties. Besides, both Zr and Te have large X-ray absorption coefficients and these also result in interesting diffraction patterns because of the self-absorption by the parent sample [56].

1.1.2 Transport Properties of Zirconium Telluride (ZrTe_5)

Research in ZrTe_5 has increased considerably since the discovery of a charge density wave (CDW) at low temperatures [8]. In such unique situations, the conceivable uses of pentatellurides like ZrTe_5 in thermo-electrics [10] have advanced a serious investigation for clarifying the beginning of their abnormal transport properties [11], in spite of having little success so far. Several mixed rare earth materials with colossal magneto resistance (CMR) have been employed in the recent past to treat non-magnetic Pentatelluride [12].

1.1.2.1 Resistivity

The resistivity of ZrTe_5 shows an important anomalous peak at T^* [2], “with an increase by factor 3 respect to its room temperature values” [31]. It has been reported that, it is conceivable to find samples of ZrTe_5 with temperature $T^* \sim 135$ K [29], $T^* \sim 140$ K [2], and $T^* \sim 170$ K [30]. It has been also observed that the values of T^* can strongly change by a controlled substitutional doping of the material [31]. Some researchers suggest that the anomalies in transport phenomena are probably due to the polaronic nature of these pentatellurides. Polarons are trapped electrons in a one-dimensional material caused due to electron-phonon interactions [13]. These polarons can form a conduction band at low temperatures that can result in a sudden resistivity peak at a particular characteristic temperature [13].

1.1.2.2 Thermopower

ZrTe₅ is known for its thermoelectric properties which are effected by its transport anomaly [31]. This resistivity peak is accompanied by a sign change in the thermopower at the same T*. The thermopower in a material quantifies the magnitude of the induced electric voltage in response to a temperature gradient across the material. In the material, the thermopower can be positive or negative. The thermopower sign is determine the nature of charge carriers, so if the charge carrier is negative, the thermopower is negative, and positive if the charge carrier is positive. Accordingly, the change of sign of ZrTe₅ thermopower could be associated with change of the charge carrier sign [31].

1.1.2.3 Positive Magnetoresistance

ZrTe₅ presents an obvious magnetoresistance (MR), “the property of a material to change the value of its electric resistance under the application of an external field” [31]. It has been reported that, by applying a magnetic field B perpendicular along to the surface b, the resistivity peaks of ZrTe₅ can be increased.

1.1.3 Topological Properties of ZrTe₅

In these last years, ZrTe₅ has likewise increased expanding consideration about its topological character [14] and has been a part of several debates in the scientific community [15]. Some reports suggest that ZrTe₅ is a Dirac semimetal that does not possess a distinctive bandgap [16], and there are several characterization techniques such as ARPES, STM, magnetic susceptibility measurements, low temperature resistivity measurements, etc. that can be employed to confirm these properties of the material [17].

ZrTe₅ is a unique topological material that is known to be insulating on one layer and conducting on the other, making it a multi-layered topological material. Sometimes, this material is a semi-metal in its bulk, i.e. in layers below the material surface while their valence and conduction bands touch at Fermi levels [18]. Depending on degeneracy of the energy bands, ZrTe₅ is sometimes called a topological Weyl semimetal. Some of the other interesting topological properties ZrTe₅ possesses are the existence of Weyl and Dirac fermions, they are high temperature superconductors, topological insulators, graphene analogues, etc. [18].

1.1.4 Topological Insulators

However, in the case of two-dimensional (2D) topographical insulators, for time-reversal symmetry, it is essential that electrons traveling in opposite directions have spins oriented in opposite directions as well in the one-dimensional (1D) edge state [18]. These topographical insulators along with Dirac and Weyl semimetals have reopened up a new surge in research on the transport properties of such interesting topographical materials [19]. Even though these transport anomalies are still mostly unclear, some groups suggest that interlayers of these semimetals play a crucial role in defining the topological behavior of these materials in bulk [20]. However, definite experimental confirmations of the topological character of ZrTe₅ is as yet uncertain [31]. The uncommon temperature advancement of the electronic transport properties of ZrTe₅ comprises in a resistivity peak at T* joined by a sign inversion of the Seebeck coefficient [3]. Seebeck coefficient S, is what is used to denote the thermoelectric power of ZrTe₅ and is defined by the equation $E = S \nabla T$, where E is the electric field generated by the crystal [3]. However, because of the impurities present and sample defects resulting from the specimen development conditions, T* depends critically on the specimen and it can shift from ~ 60 K to ~ 170 K. The source of these confusing properties

has been subject of significant research and diverse systems including a basic stage change, development of charge density waves (CDW) and the nearness of polaronic charge bearers have been considered [26]. However, straightforward experimental confirmations supporting these speculations are yet missing, and a consistent agreement about the behavior of its band structure versus temperature has not yet been determined.

Studies on the electronic band structure of the material has uncovered a shift in the band towards lower $E - E_F$ energy states, which was monotonic in the researched temperature scope of 300 – 125 K. Specifically, the energy of coupling of the characteristic Dirac cone at the Γ point of the Brillouin zone achieves its pinnacle at $\sim T^*$. The electronic properties of $ZrTe_5$ are governed by the valence and conduction band branches that have almost a linear dispersion at the center of the Brillouin zone [19]. The Γ point as discussed above, is basically a small spot on the center of the Brillouin zone that is depicted as a constant energy contour at the Fermi Level in an ARPES data plot. There are also bands at the Brillouin zone boundaries that crosses the Fermi levels at low temperatures when the momentum space of the Brillouin zone is mapped [19]. There are no other energy bands observed over the Brillouin zone at any other temperatures and these bands around the Brillouin zones are what result in the interesting topological properties of $ZrTe_5$ [5].

1.2 Applications of Zirconium Telluride

Quantum Hall states belong to a topological category of materials that cause a rupture on the time reversal symmetry in the presence of external magnetic fields [14]. A topological insulator (TI) [14] can improve the electronic transport inside a bulk insulator, which are topologically secured. In two-dimensional (2D) TIs, in particular, the quantum spin Hall

(QSH) separators [14], the low-energy (back) scrambling of the boundary states are denied by the time-inversion symmetry that causes transport edge channels and the QSH effects [14]. Several experimental results confirmed how 2D topological insulators showed quantum hall effect in some telluride quantum wells [14]. However, the known experimental verifications of the QSH impact in HgTe/CdTe quantum-well structures require extreme synthesis conditions like the precisely controlled molecular beam epitaxy (MBE) and the ultralow temperature because of the bulk bandgap of the levels of a few meV, which extremely prevents additional test studies and conceivable applications [14].

To be a "decent" quantum spin hall insulator, the material must meet the accompanying critical criteria: (1) It must be a decent layered material to effectively acquire the chemically stable 2D framework; (2) it must have an expansive 2D mass bandgap to figure it out the QSH impact at high temperatures [14]. The principal proposition of graphene as a QSH separator is basically futile in light of its amazingly small gap (10^{-3} meV) instigated by spin-orbit coupling (SOC) [14], albeit, up until now, graphene is the best 2D material and that be effectively made even by the scotch-tape technique [14]. As of late, Bi₂TeI has been proposed as another possibility for a QSH insulator [14] even though it has a small bandgap. The bismuth (111) bilayer is conceivably a substantial bandgap (around 0.2 eV) QSH cover [14]. In any case, its interlayer holding is solid, and its synthesis is difficult [14]. A few different propositions such as ultrathin tin films and the Cd₃As₂ quantum well have a similar issue. Since they are not layered materials, the very much controlled molecular-beam-epitaxy (MBE) system is required to acquire the ultrathin-films. These films, because of their different transport properties at different layers can then be employed in several practical applications in electronics as well due to its conductivity similar to that of graphene layers [14]. These

topological properties and Quantum spin Hall effects properties make ZrTe_5 particularly useful in spintronic devices and quantum computing [18].

1.3 Potential Applications as Double Layered Thermoelectrics

Straightforward double layered pentatellurides like ZrTe_5 , already known as layered thermoelectric materials, are interlayer feebly reinforced materials equivalent to graphite [14]. Their single-layer sheets, which can be made, on a basic level, without MBE, are QSH protectors with a vast mass hole, and they are powerful against cross section mutilations [14]. Along these lines, ZrTe_5 is a very promising 2D TIs that fulfill both of the above conditions and clear another route to facilitate test examines the effects of QSH [14]. Also, certain estimations demonstrate that the three-dimensional (3D) crystals shaped by the stacking of layers are situated in the region of a progress amongst solid and powerless TI, additionally making them an ideal stage to consider the topological quantum-stage changes [14].

CHAPTER 2: Experimental Materials

In this study, the crystal growth of ZrTe_5 is attempted through a known recipe. The elemental composition of the different crystals is also assessed through, X-Ray Diffraction, X-Ray Photoelectron Spectroscopy and Scanning Electron Microscopy.

2.1 Raw Materials

ZrTe_5 was synthesized by taking pure Zr (Alfa Aesar- 3N) with Te source elements (Alfa Aesar- 6N) and high purity of transport agent “ I_2 ”. The high purity of ampoules was prepared by a glass blower Aaron Babino [51].

2.2 Crystal Growth

ZrTe_5 crystals were grown by a chemical vapor transport method (CVT). The materials were loaded into a sealed and evacuated ampoule that placed in a furnace in horizontal position to grow the crystals. The furnace was heated to 520 and 450 °C respectively to growth the crystals. The crystals with a metallic sheen were successfully obtained after growing in the temperature gradient for over 10 days [51].

2.3 Growth Mechanism

Schematic in figure 2 (a) displays the chemical vapor transport (CVT) growth furnace. In the beginning, temperature adjustment is carried out on the furnace [51]. In order to maintain crystal growth, the mixture of ZrTe_5 together and specific quantity of the transport agent are placed at the hot zone of the tube (T_2). Also, as an avenue for crystal growth, the end of the tube is kept at the low temperature (T_1). “The raw materials and transporter may be volatilized in the form of a chemically intermediate phase at a high temperature”. The

chemical intermediate decays and forms ZrTe_5 nuclei and compress at the internal surface of the tube as seeds when the intermediate phase diffuses to the lower temperature growth area. Next, ZrTe_5 vapor molecules combine the seeds, and the seeds slowly grow into single strip crystal as shown in figure 2.1 (b). This growth is ruled by an intrinsic property of the material which causes different growth rates along different directions. The growth along the a -direction is the fastest, followed by c , and b , respectively with the $a - c$ plane growing into the surface that is exposed dominantly [51]. Finally, high crystalline ZrTe_5 can be growth after adjusting the growth parameters such as the concentration of the transport agent, the temperature gradients, and the shape of the tube [51].

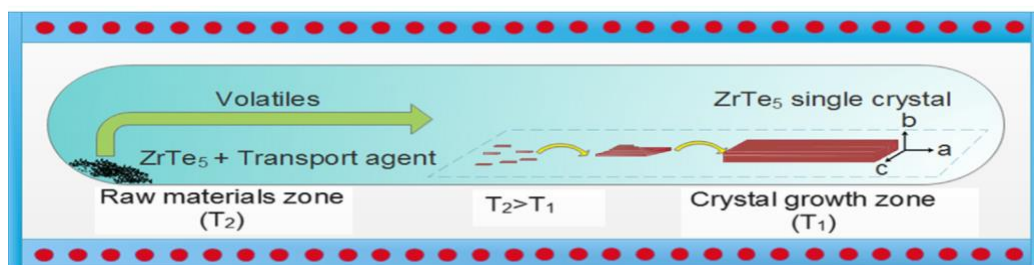


Figure 2.1 (a) schematic shows the CVT growth furnace of ZrTe_5 single crystal. (b) Picture of the grew up of ZrTe_5 single crystals on the internal surface of the tube.

2.4 The Usage of Nitrogen

Before taking the samples out for further characterization, Nitrogen gas was employed to get rid of iodine and also to clean them. Nitrogen is a non-reactive gas. It is an abundant, stable gas that has several commercial and biological properties that can be exploited in the synthesis of several materials as well as by industries. In the synthesis of several materials, nitrogen provides an inert environment that prevents the oxidation of samples. It is also useful in getting rid of different unstable organic compounds that maybe a side effect of various synthesis processes. Also, it can be used to clean and reduce different toxic materials in a reaction solution or in a gaseous phase [65].

2.5 Calculations for Producing $ZrTe_5$

In this study, seven samples were prepared to grow Zirconium Pentatelluride. Those samples have different Zr concentrations, Te concentrations and I “the transport agent” concentrations to grow successful and high quality of $ZrTe_5$ crystals. The ratios of those samples were different. In the first sample, we took a piece of the Zr and measured. Then, we calculated the Te by using that measurement; however, the material for sample 2,3 were five times, and ten times smaller than the first try. Sample 4 was by using half the amount of the ratio that has mentioned in the reported work [51]. For samples 5 and 6 the concentrations were decreased gradually to have long seeds of $ZrTe_5$. However, in the last sample, the concentration of $ZrTe_5$ was 2 grams as mentioned in Lv’s work [51], whereas the transport agent concentration was decreased to 1.2.

Concentration Sampels	Mass of Tellurium (Te) g	Mass of Zirconium (Zr) g	Mass of Transport agent (I ₂) g
First attempt	1.22	0.0174	1.7
Second attempt “less 5 times”	0.244	0.0174 g	0.34
Third attempt “less 10 times”	0.122	0.0174	0.17
Fourth attempt (1 g)	0.877	0.123	1.7
Fifth attempt	0.469	0.067	0.9
Sixth attempt	0.05	0.361	0.7
Last attempt (2 g)	1.754	0.246	1..2

Table 2.1: Calculations for producing ZrTe₅

CHAPTER 3: Experimental Technique

3.1 Crystal Characterization

ZrTe₅ samples were characterized by X-ray diffraction using Cu-K α radiation as an X-ray source at a scan rate of 0.6° per minute, and the 2 θ scanned was from 10°-70°. The synthesized ZrTe₅ samples were also investigated by XPS (X-ray photoemission spectroscopy), and by SEM scanning electron microscopy [51].

3.1.1 X-Ray Diffraction (XRD)

In last few years, X-ray diffraction (XRD) has become an important technique for examining the properties of the fundamental studies and crystals structure and polymers [31]. It is a powerful nondestructive technique for characterizing crystalline materials [38]. It gives information on crystal structure, phase, preferred crystal orientation, and other structural parameters, such as average grain size, crystallinity, strain, and crystal defects [38]. Around 95% of solid material can be described as crystalline [38]. At the point when x-rays collaborate with a crystalline substance, one gets a diffraction design [32]. In 1919 A. W. Hull gave a paper titled, "A New Method of Chemical Analysis" where he highlighted that each crystalline substance gives a specific pattern; a similar material dependably gives a similar pattern, and an independent set of patterns are created in a mixture of materials [33].

Diffraction patterns are obtained when electromagnetic radiation falls on crystalline structures with geometrical arrangements in length of the same order as that of the wavelength of the incident radiation. The interatomic spacing in crystalline solids and molecules are about 0.15– 0.4 nm, which is about the same as the wavelength of x-rays in the electromagnetic range having photon energies of 3 - 8 keV. As is the case, processes like the constructive and

destructive interference are fairly conceivable when crystalline and molecular structures are subjected to x-rays [57]. Before the geometrical requirements for x-ray interference are determined the influence of x-rays on matter must be considered. There are three unique sorts of collaboration in the significant energy range [57]. In one form of interaction, electrons might be freed from their bound nuclear states during the time spent photoionization. Since energy and momentum are exchanged from the approaching radiation to the energized electron, photoionization falls into the gathering of inelastic scattering forms [57]. What's more, there exists a different sort of inelastic scattering that the incident x-ray radiation may experience, which is named Compton scattering. Likewise, in this Compton scattering, energy is exchanged to an electron, which continues, however, without discharging the electron from the atom. At last, x-rays might be scattered elastically by electrons, which is named Thomson scattering [57]. In this last procedure, the electron wavers like a Hertz dipole at the recurrence of the incident radiation and turns into a source of dipole radiation. The wavelength λ of x-rays is saved for Thomson scattering as opposed to the two inelastic scattering forms specified previously. It is the Thomson segment in the scattering of x-rays that is made utilization of in basic examinations by x-ray diffraction [57].

3.1.1.1 Powder X-Ray Diffraction

In X-ray diffraction work we regularly recognize single crystal and polycrystalline or powder samples. The powder diffraction technique is a preferably suited for sample characterization and recognizable proof of polycrystalline stages [35]. Today around 50,000 inorganic and 25,000 organic single part, crystalline, diffraction designs have been gathered and recorded in different online and offline databases. The principle utilization of powder diffraction is to distinguish parts in a specimen by a search/match strategy. Moreover, the

regions under the peaks are identified with the contribution of each phase present in the specimen [38]. In powder or polycrystalline diffraction, it is imperative to have a sample with a smooth plane surface. Generally, large, chunky samples are ground down into finer particles with sizes of around 0.002 mm to 0.005 mm cross area [57-59]. The perfect sample is homogeneous also, the crystallites are randomly oriented so that intensity ratios can be analyzed accurately for quantitative purposes. This quantitative analysis will not be possible if the crystals are not randomly distributed because there will be a definite change in the intensity ratios that would affect further calculations [57-59].

The specimen is squeezed into a sample holder with the goal that we have a smooth level surface. In ideal measurement conditions, we now have random distribution of all conceivable h, k, l planes. Just crystallites having reflecting planes (h, k, l) parallel to the example surface will add to the reflected powers. On the off chance that we have a really arbitrary specimen, every conceivable reflection from a given arrangement of h, k, l planes will have an equivalent number of crystallites adding to it. We just need to shake the example through the looking point θ to create all conceivable reflections [57-59].

3.1.1.2 Single Crystal X-Ray Diffraction

The single crystal samples are perfect (all unit cells adjusted in an impeccable geometric pattern) crystals with a cross segment of around 0.3 mm [58]. The single crystal diffractometer and related software is utilized for the most part to illustrate the crystal structure of specific compounds, either naturally occurring or man-made materials [58]. The samples are undivided and optically transparent single crystals. Their size ought to be between 0.1 and 0.2 mm in a 3D orientation [58]. They are typically chosen utilizing a simple optical

microscope, magnified to about 40x, loaded with a polarizing accessory and observing if light disappears consistently every 90° when turning the translational phase of the magnifying lens.

The structure parameters are reciprocal lattice vectors though the electron density is from the real space. The diffraction pattern is the Fourier transformation of the electron beam and the electron density is the converse Fourier transformation of the diffraction pattern [59]. The slow forces of a diffraction pattern allow the assurance of just the structure factor amplitudes but not their specific phases [59]. The computation of the electron density isn't at that point obtained directly from experimental estimations and the phase values must be acquired through different strategies. This is the apparent phase issue. The most common techniques to beat the phase issue are immediate techniques and techniques in view of the Patterson function. The previous are the most essential in X-ray crystallography and the latter are right now used when analyzing materials involving heavy atoms [59]. The phases are acquired approximately and must be refined. With the figured phases and structure factors amplitudes, at first an electron density map is determined from which the specific atomic positions can be calculated [59].

3.1.2 X-Ray Photoelectron Spectroscopy

In this study, X-ray photoelectron spectroscopy is applied to investigate the chemical elements and the binding energy of the compound. X-ray photoelectron spectroscopy is a surface characterization technique analysis. It shows the nature of the chemical bond that exists between the elements and the chemical elements which are existing at the surface. A monochromatic beam of high-energy photons (X-rays) strikes on the example to be considered, energizing an electron in the specimen to a higher energy excited state [39]. On the off chance that the energized state is higher than the "vacuum level" of the specimen (the sum of the Fermi energy and the work function), the electron might be launched out into the vacuum and gathered and energy examined by the electron spectrometer [40]. With information on the last state electron energy and the energy of the x-rays, energy preservation at that point enables us to conclusively decide the underlying state energy of the electron before it was ejected from the specimen, utilizing the condition $E_k = hv - BE - \phi$ where E_k is the kinetic energy of the electron ejected from the surface, hv is the photon energy, BE is the binding energy of the electron in the sample, and ϕ is the work function [41]. The peak as a component of energy in this manner let us know the compound components in the specimen that the electrons were launched out from. The quality or intensity of the peaks is relative to the quantity of particles of any sort from which the electrons are launched out so that the stoichiometry of an unknown sample can be distinguished, as well as the valence of the chemical composition of the inner elements. Eventually, the surface sensitivity (in the region of 5-50 Å) permits a novel perspective of the physical and chemical properties of the material surface [42].

3.1.3 Scanning Electron Microscope

A scanning electron microscope (SEM) is a sort of electron microscope that creates images of a sample by scanning the surface with a concentrated beam of electrons. The interaction of electrons with atoms in the sample produces several signals that have information about the sample's surface external morphology and chemical composition. To produce an image, the electron beam is scanned in a raster scan pattern, and the beam's position is merged with the revealed signal. In conventional SEM, samples can be observed in high vacuum, or in low vacuum or wet conditions and at a broad range of low or high temperatures with particular instruments [43].

The detection of secondary electrons emitted by atoms which excited by the electron beam is the most common SEM mode. The number of secondary electrons that can be detected be contingent among other things on sample topography. Finally, an image displaying the topography of the surface can be created by scanning the sample and collecting the secondary electrons that are emitted using a special detector [43].



Figure 3.1 shows the sample inside SEM instrument.

CHAPTER 4: Results

4.1 X-Ray diffraction:

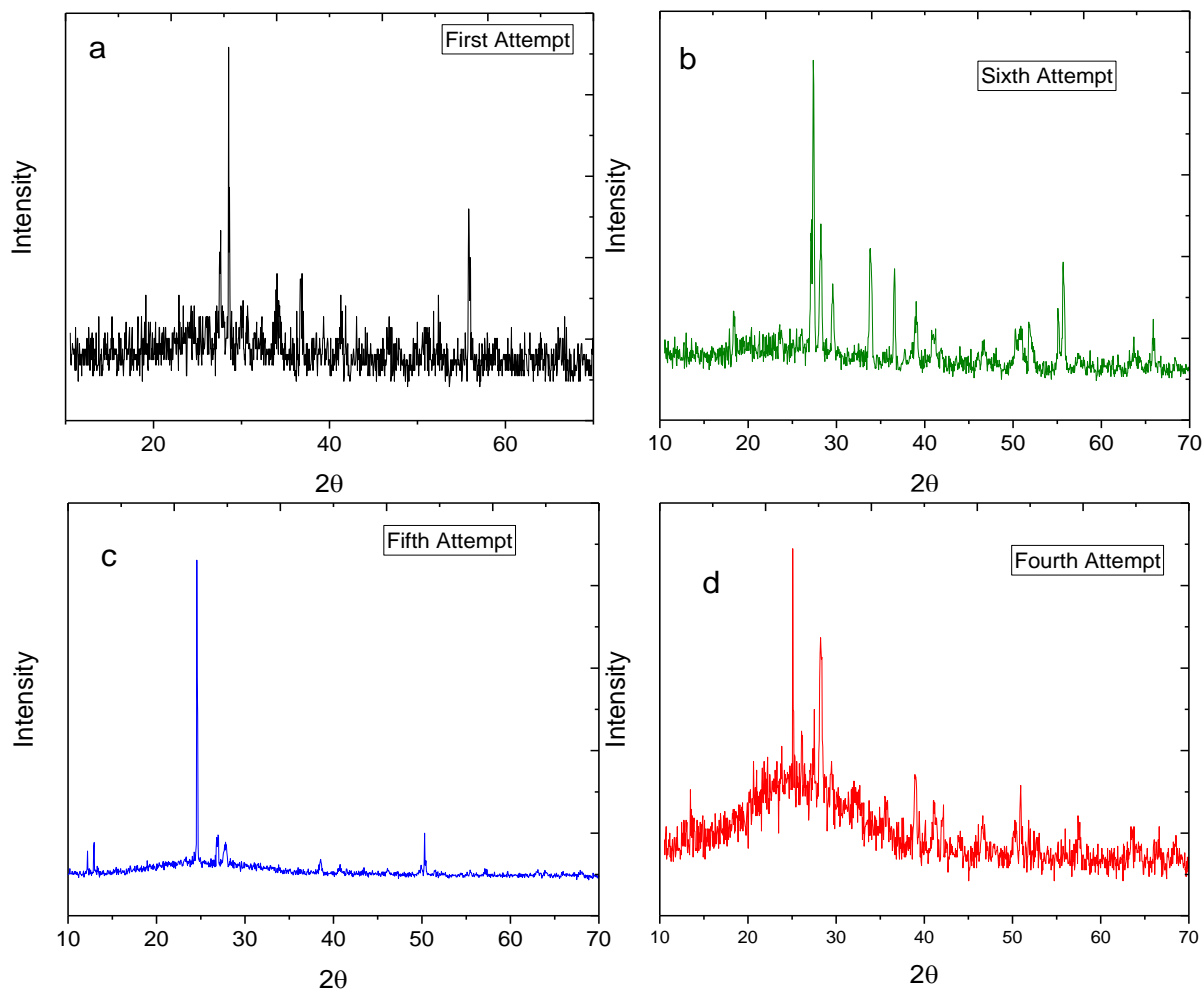


Figure 4.1 X-Ray diffraction patterns of (a) first attempt, (b) sixth attempt, (c) fifth attempt, and (d) fourth attempt respectively

Displayed in figure 4.1 (a) is the first attempt when the concentrations are Zr: 0.017, Te: 1.22 and I: 1.7. The XRD diagram comprises of 8 sharp peaks between 15° and 65° and several broader low intensity peaks as well in this range. However, these peaks do not match with the ICSD database for any form of ZrTe_5 .

Sixth attempt is shown in figure 4.1 (b) the peaks are observed at 18° , 26° , 27° , 29° , 33° , 36° , 49° , and 51° could be assigned to the ZrTe_5 . Figure 4.1 (c) was closest to the reported form of ZrTe_5 powders and with the standard database (ICSD Code: 085506). Figure 4.1(d) presents the fourth attempt which is fairly noisy with prominent peaks appearing at 27° , 39° , 40° , 42° , 50° , and suggesting a powder ZrTe_5 phase might be present.

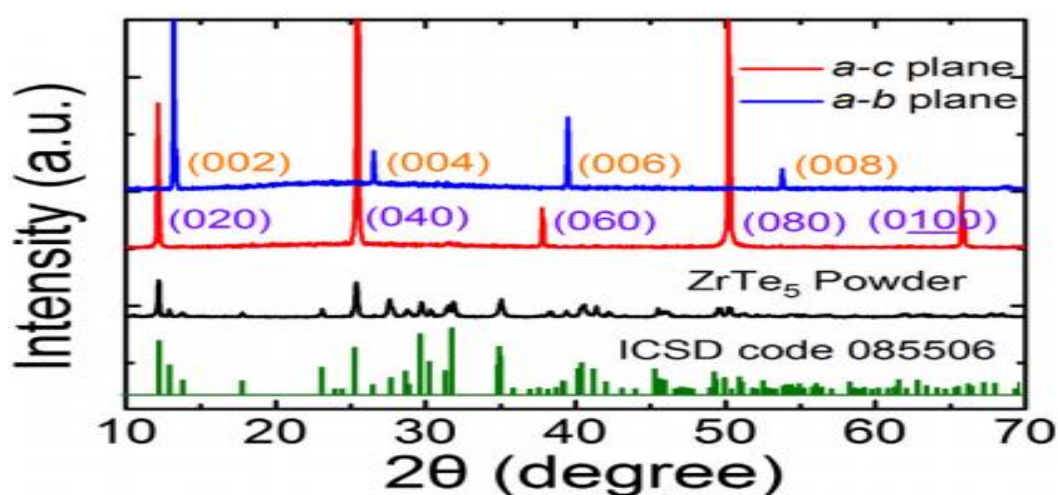


Figure 4.2 Standard XRD patterns, powder XRD patterns and single crystal XRD patterns (measured on *a-c* and *a-b* planes, respectively) of ZrTe_5 samples, respectively [51].

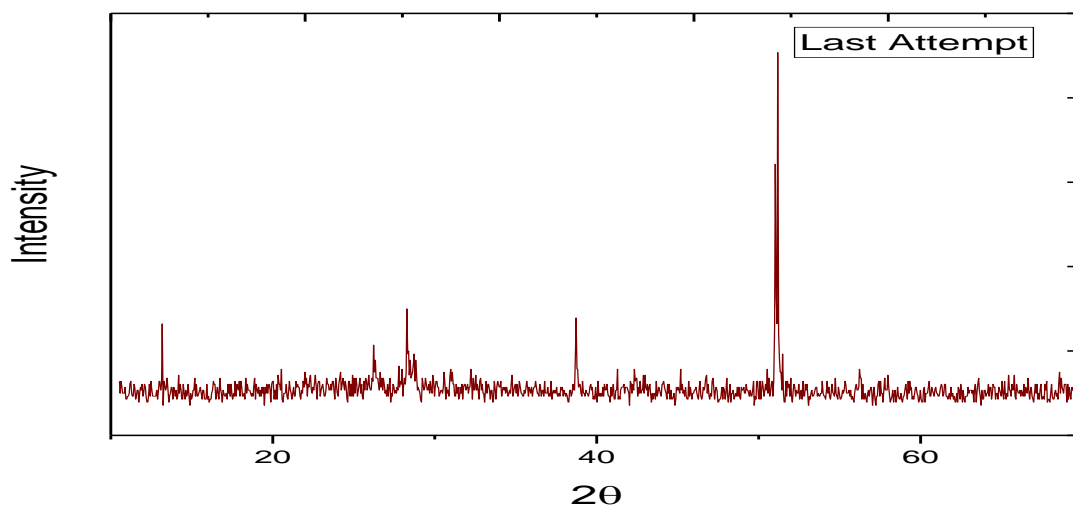


Figure 4.3 X-Ray diffraction pattern of the last attempt

Presented in figure 4.3 is the last attempt for ZrTe_5 growth. The peaks corresponded to the $0k0$ planes that were characteristic for $a - c$ as the maximum exposed surface of the crystal. These peaks can be assigned as (020) , (040) , (060) , (080) , and (0100) for 2θ values are about 13° , 26° , 38° , 51° and 65° , respectively. The peak at 65° is supposed to have the same relative intensity as the peak at 65° in the reported work, while the other intensities are the same.

4.2 X-Ray Photoelectron Spectroscopy (XPS):

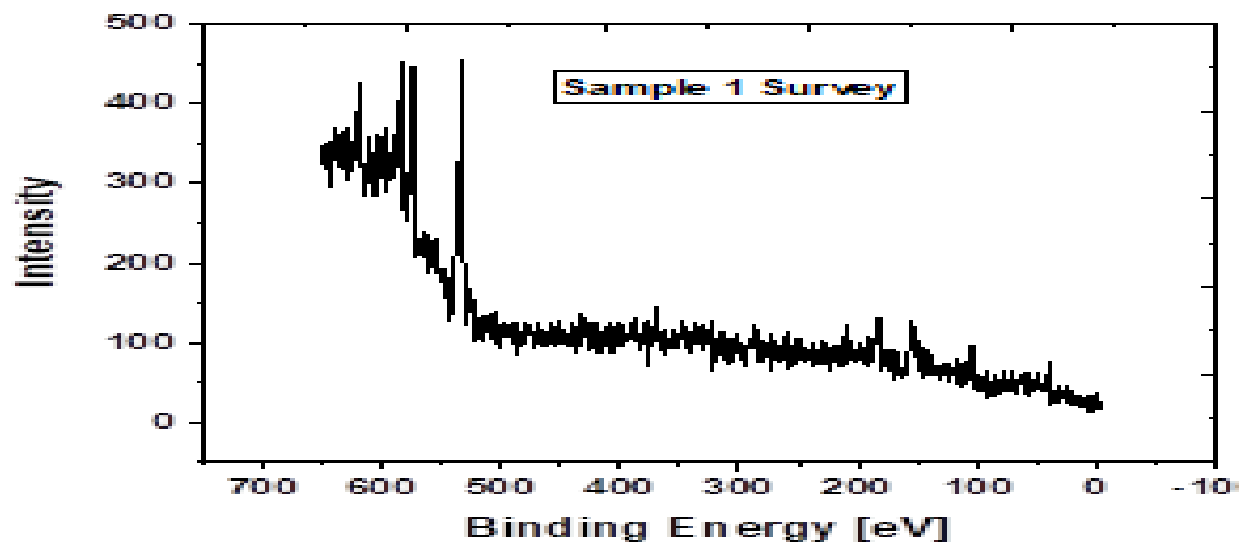


Figure 4.4 XPS survey spectra of the sample with Zr = 0.0675 and Te = 0.469 for the binding energy range between 0 – 700 eV and the characteristic peak of Zr, Te, O, and C

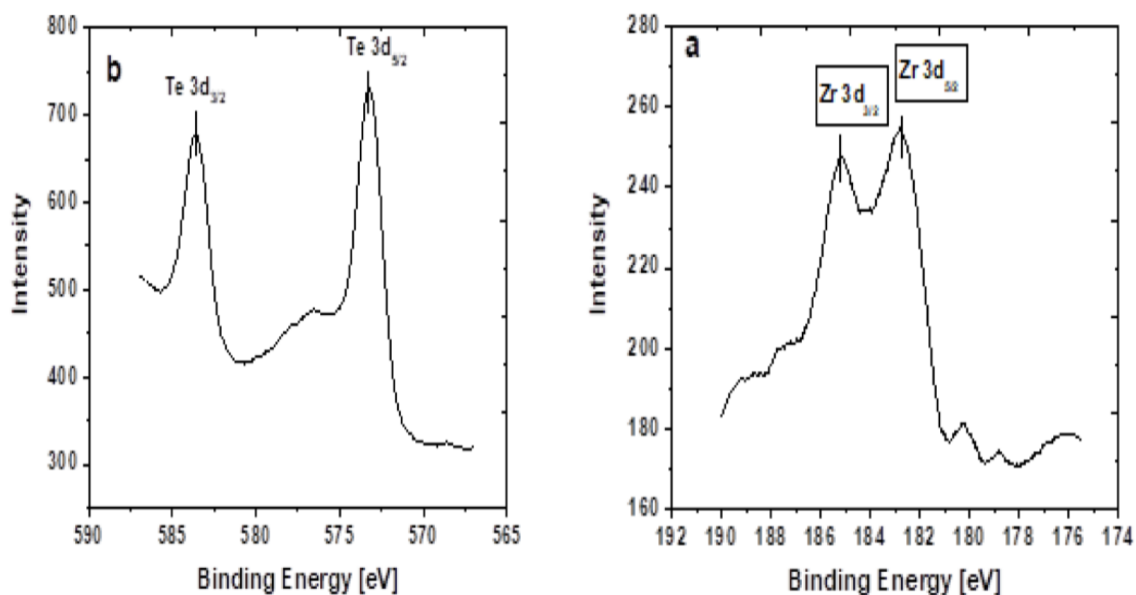


Figure 4.5 High-resolution XPS of (a) Zr and (b) Te, of the sample. Figure.2 (a) shows the high-resolution XPS of the Zr 3d sample and the characteristic 3d_{3/2} and 3d_{5/2} doublet of Zr that is present at 182.7 and 185.2 eV, respectively. Figure.2 (b) shows the high-resolution XPS of Te and the characteristic doublet of 3d Te, 3d_{3/2}, and 3d_{5/2} which exists clearly at 573.2 and 583.5 eV.

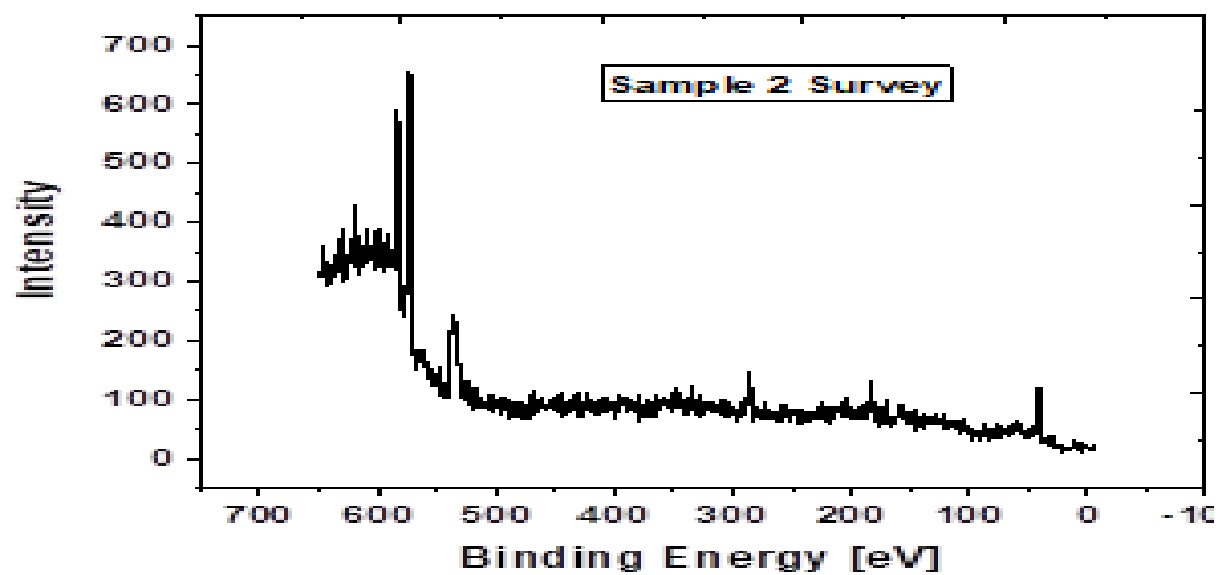


Figure 4.6 XPS survey spectra of the sample 2 with Zr = 0.05 and Te = 0.361 for the binding energy range between 0 – 700 eV, and characteristic peaks of Zr, Te, O and C

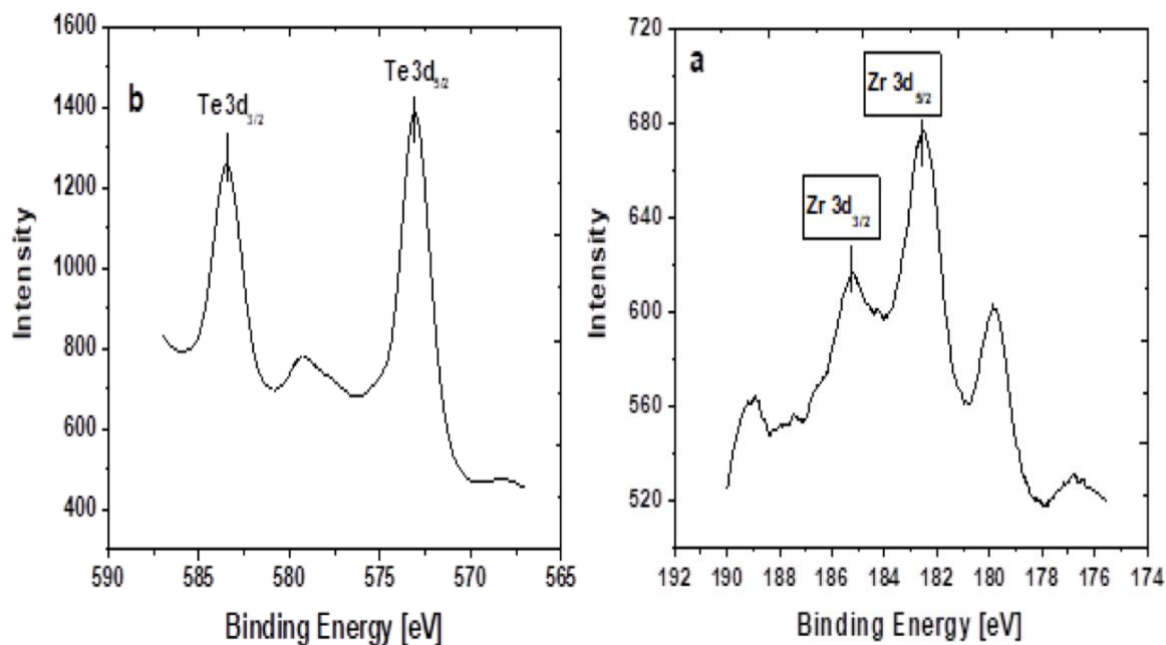


Figure 4.7 High-resolution XPS of (a) Zr and (b) Te, of the sample. Figure 4.7 (a) demonstrates the high-resolution XPS of the Zr 3d and the characteristic $3d_{3/2}$ and $3d_{5/2}$ doublet of Zr which can be seen at 182.5 and 185.2 eV. Figure 4.7 (b) shows the high-resolution XPS of Te and the characteristic doublet of 3d Te, $3d_{3/2}$, and $3d_{5/2}$ that present at 573 and 583.5 eV, respectively.

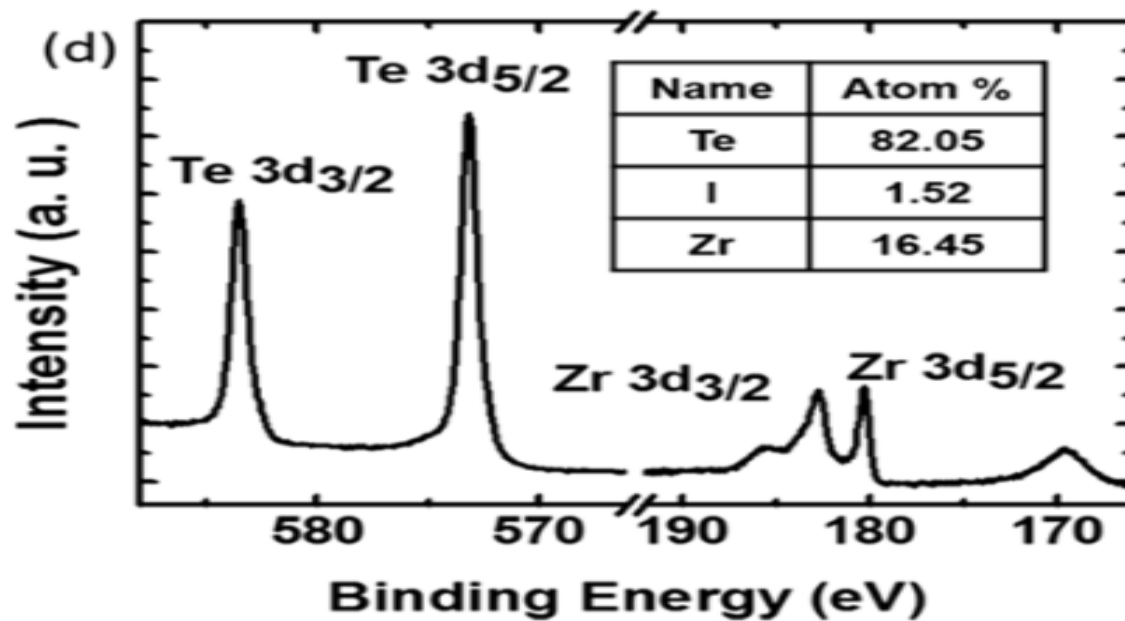


Figure 4.8 X-ray photoemission spectroscopy (XPS) results of binding energies of Zr and Te. The inset table summarizes the atomic ratio of measured sample [64].

4.3 Scanning Electron Microscope (SEM):

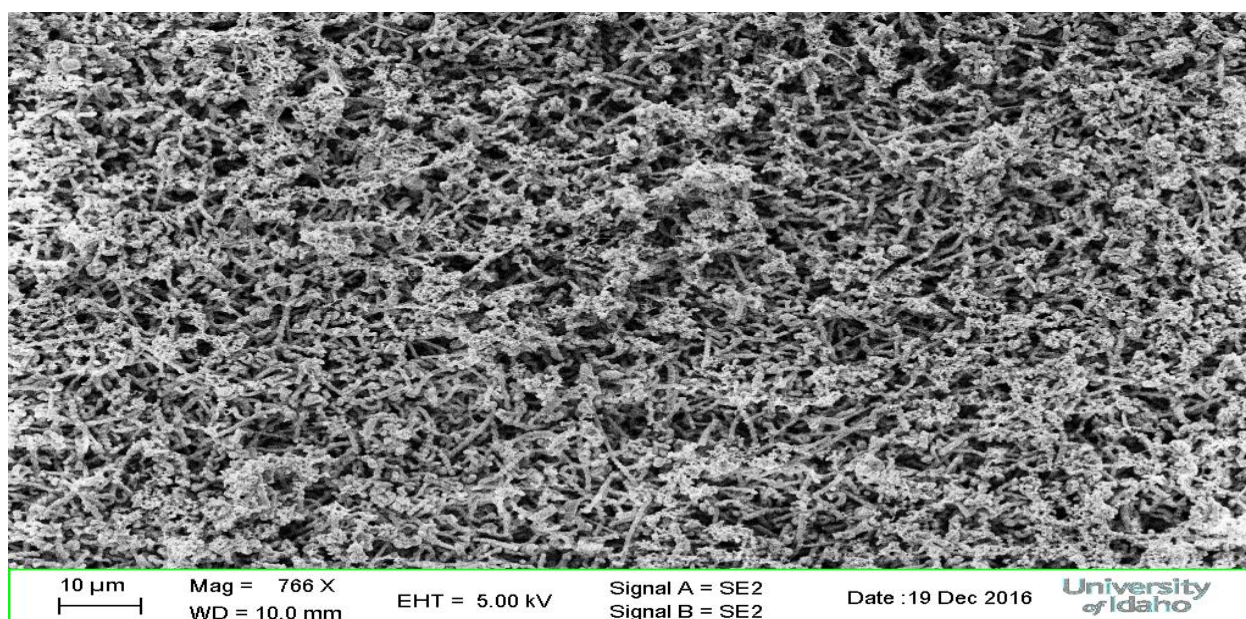
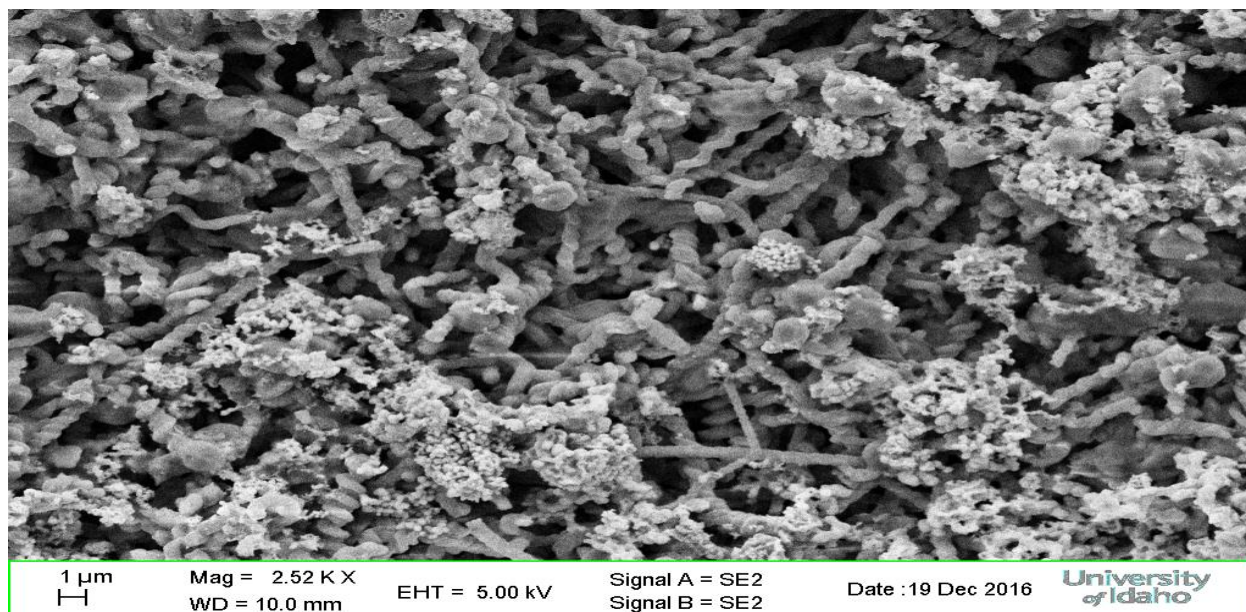


Figure 4.9: The first attempt of growing nanosprings on a chip of silica.

Figure 4.9 presents two SEM images of nanosprings viewed at 2.52 k x and 677 x magnification with Zr; Te concentrations of 0.0174 g and 1.22 g respectively. It can be clearly seen that, although there are nanosprings in both images, they are not uniform and did not form very well.

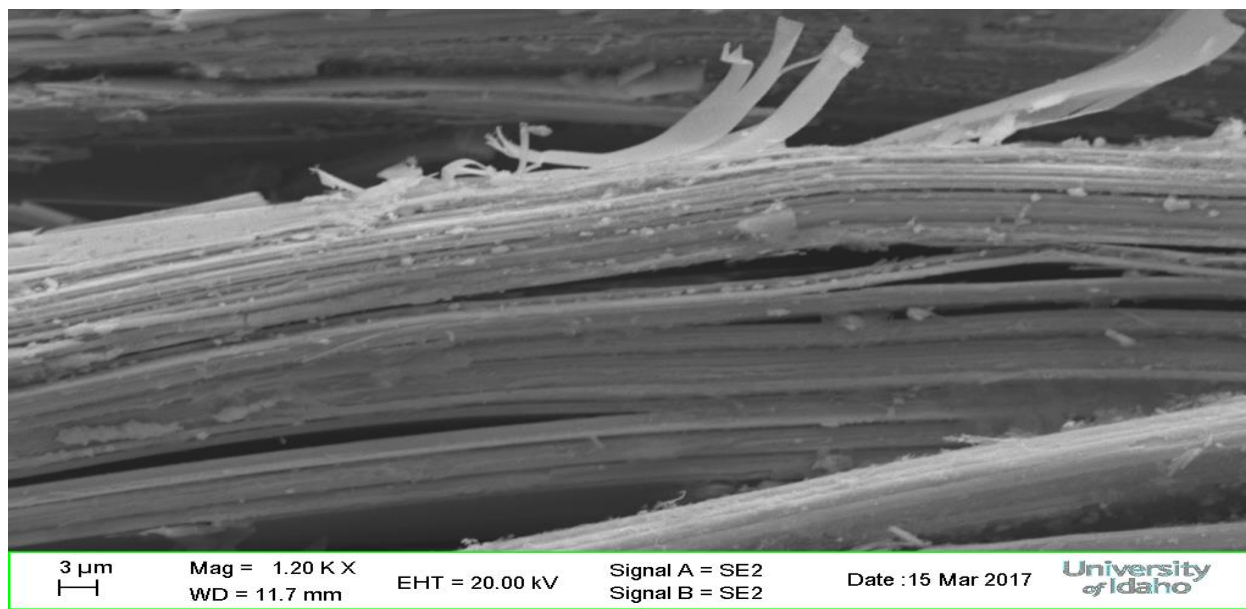
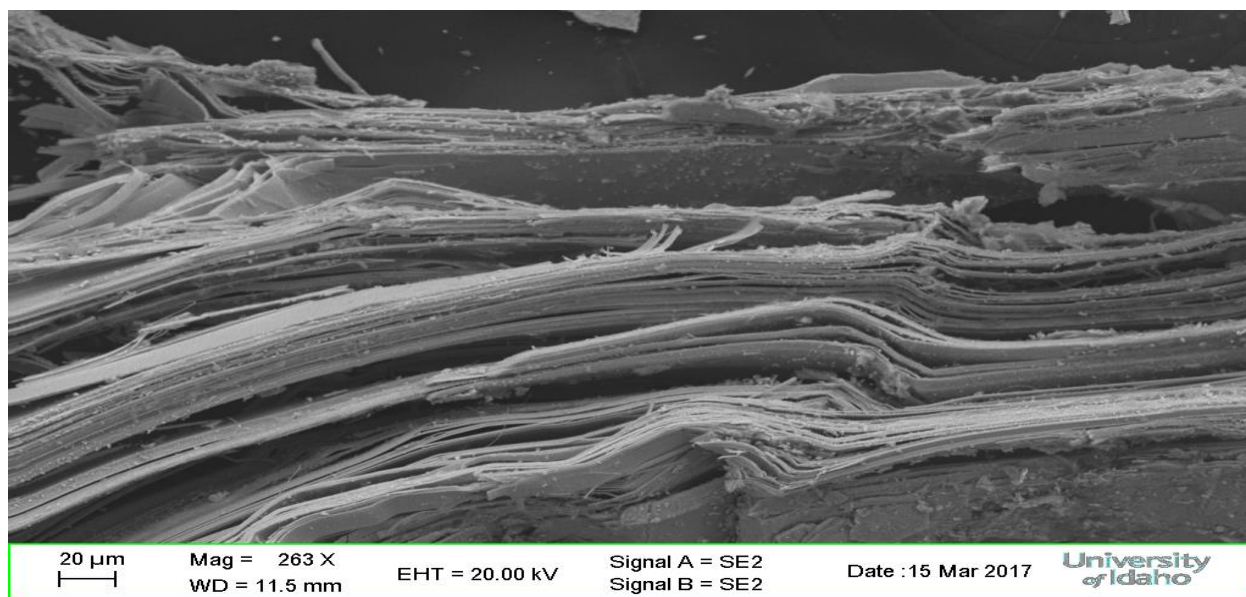


Figure 4.10: a SEM image for the sixth sample of growing ZrTe₅



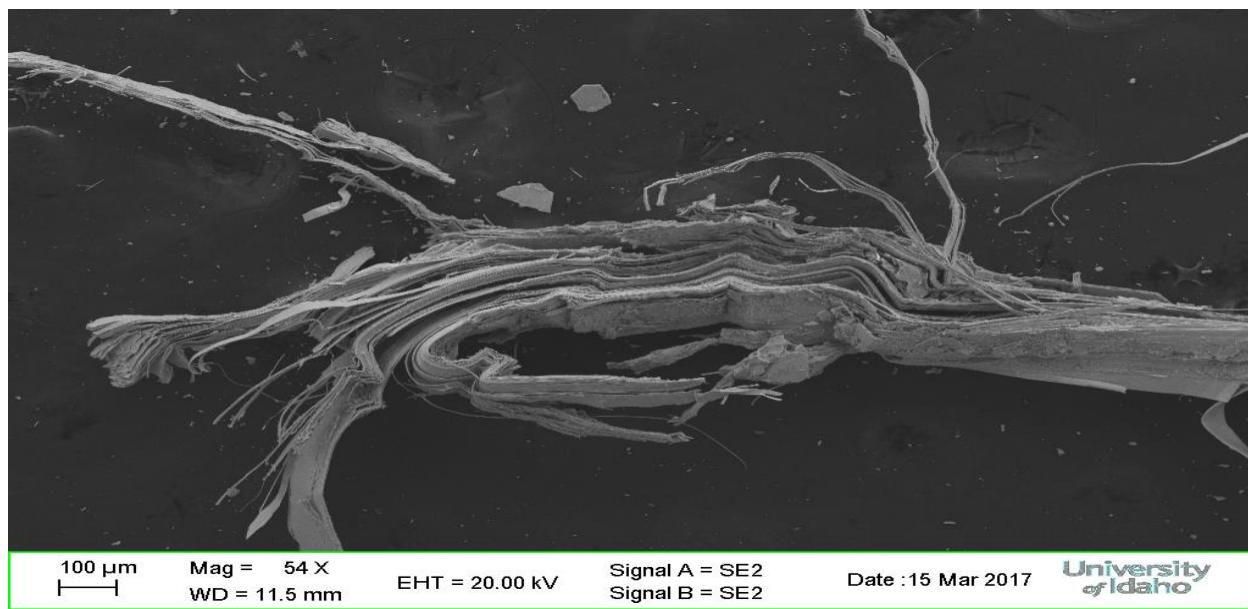


Figure 4.11: The layers of ZrTe₅ for the sixth sample in different magnifications

Displayed in Figure 4.10 is a SEM image of the layers of ZrTe₅ at 1.20 k x magnification with Zr; Te concentrations of 0.05 and 0.36 g respectively. We can obviously see the very uniform layers of ZrTe₅ that are stacking on top of each other, and we can also notice some layers are peeling off.

Illustrated in figures 4.11 is the SEM images of ZrTe₅ at 54 x and 263 x. The first image shows some layers of the zirconium telluride are peeling off, and the second image displays its uniform layers.

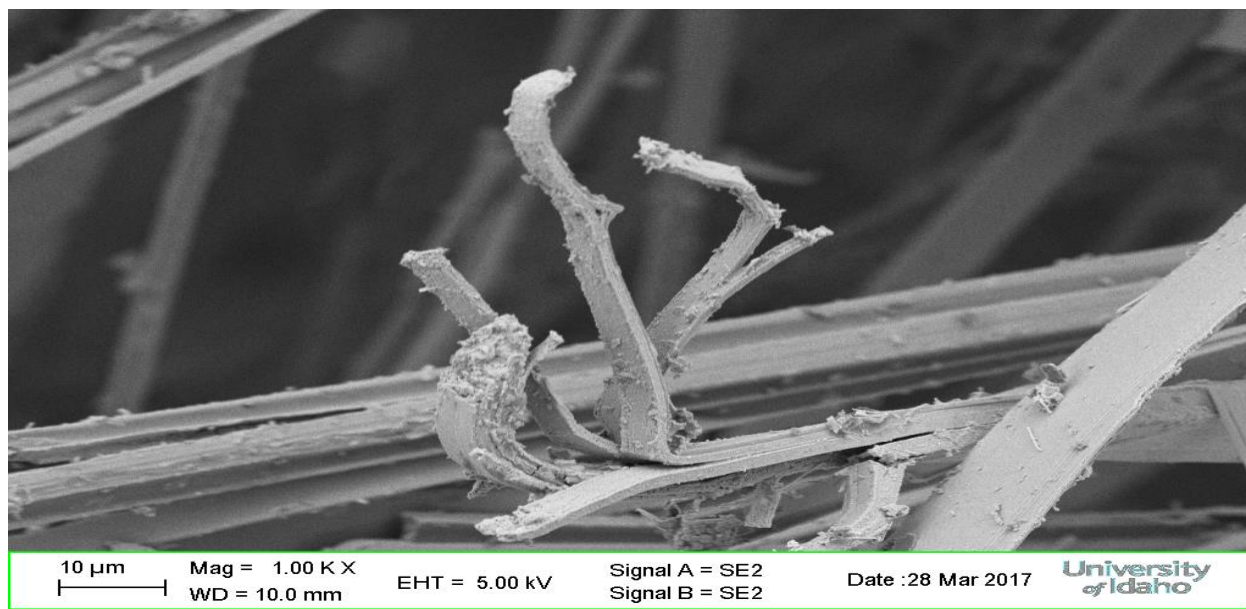


Figure 4.12: The fourth attempt of growing $ZrTe_5$ when Zr:Te is 1 g.

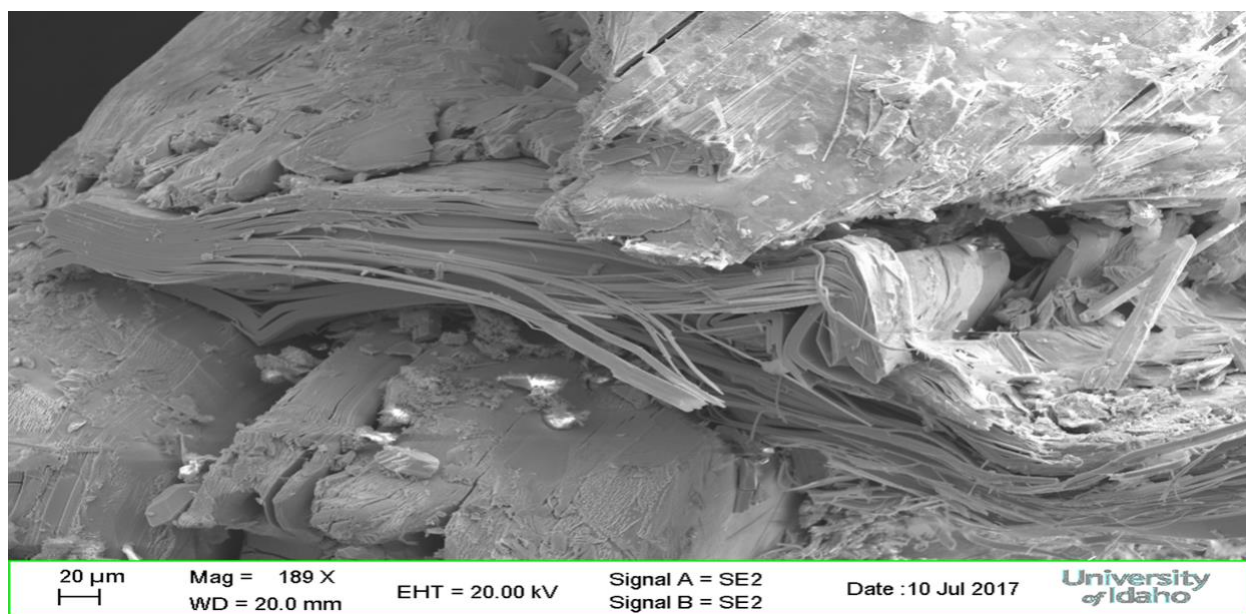


Figure 4.13: The last attempt of growing $ZrTe_5$ when Zr: Te is 2 g.

Demonstrated in Figure 4.12 is the SEM image of ZrTe_5 at 1.00 k x magnification with Zr; Te concentrations of 0.246 g and 1.75 g respectively. It is difficult to see the layers, but it has a uniform coating as expected.

The displayed figure presents the last attempt of growing ZrTe_5 when the concentration of the transport agent increased to 1.2 g while the mixture of Zr; Te was 2 g. It can be observed that some parts are layer by layer while other parts are very dense.

CHAPTER 5: Discussion

5.1 Procedure of the Crystal Growth

The samples were synthesized in different conditions to have long and successful ZrTe₅ crystals. Initially, the first synthesis was unsuccessful because of the excessive amount of iodine and Te. Although it coated nanosprings, they did not form very well. The experiment was repeated for 2 samples with iodine and tellurium concentrations reduced to about 5 and 10 times than their initial level. Once again, the results proved there is no ZrTe₅ in those samples which could be due to the temperature gradients. Another attempt to grow ZrTe₅ crystals was to adjust the temperature start point of from 450 °C to 520 °C. This attempt did not grow ZrTe₅. Last try was to change the shape of the ampoule. In the previous samples, Zr was placed in the middle of one side while Te and the transport agent were added to the other side in no particular order. A chip of silica was placed at the end of each ampoule in order to coat nanosprings. Eventually, the shape of the ampoule was changed to an elongated ampoule with a certain measurement that was about 3 cm in diameter and 12 cm long. This method grew so ZrTe₅, but did result in short seeds.

The next target was to grow long seeds of ZrTe₅. Programming the furnace temperature was the first attempt. The furnace was programmed to change the temperature gradually and automatically without any manual supervision. It was programmed at 520 °C and 450 °C respectively for 10 days before allowing them to cool and removing the samples from inside. Unfortunately, long seeds were not obtained in this way. Thus, it was assumed that a slight increase in transport agent level could play a role in growing the seeds. This assumption was built because it was observed that in one of the samples when the transport agent was 0.9 g, it

grew longer seeds than when it was 0.7 g. Eventually, long seeds were successfully grown when the transport agent was 1.2 g.

The successful growth of ZrTe₅ was achieved with 1.2 g of I₂, 1.754 g of Te, 0.246 g of Zr in the ampoule shape that was elongated and a temperature profile that started at 520° went from 520° to 450° C respectively in 10 days, and then from 370 to 300 for one day and then from 220 to 150 for one day as well, then the sample stayed in the room temperature for a day.

5.2 X-Ray Diffraction

In this study five samples were characterized. First, 4.1 (a) is the first attempt of growing ZrTe₅. The XRD diagram comprises of 8 sharp peaks between 15° and 65° and several broader low intensity peaks as well in this range. However, these peaks do not match with the ICSD database for any form of ZrTe₅. Therefore, it is difficult to assign them to any hkl values. This attempt did not grow ZrTe₅ which could be due to the excessive amount of Te and the transport agent or the present of nanosprings on the surface of the sample. The full width at half maximum (FWHM) of the XRD peaks gives a very good estimate into the material crystallinity and also helps calculating the crystallite size using the Debye-Scherrer formula:

$$D_p = \frac{0.94\lambda}{\beta_{1/2} \cos \theta}$$

where λ is the X-ray wavelength which is 1.54 Å, $\beta_{1/2}$ is the FWHM, and θ is the diffraction angle. The FWHM of the most intense peak at 28° can be used to calculate the crystallite size which we calculated the size as 97 nm.

In fig 4.1(b), peaks are observed at 18° , 26° , 27° , 29° , 33° , 36° , 39° , 49° and 51° , all these peaks could be assigned to the ZrTe_5 powder phase [51]. The average crystallite size for this sample was calculated as 54 nm based on the peak information of the most intense peak at 26° . These peaks probably suggest the growth of the material in no specific direction since there appears to be a random distribution of all diffraction peaks. The different cell parameters of ZrTe_5 was originally calculated by Fjellvåg and includes a, b, and c values including the cell volume. These values were experimentally verified by several others as well [53-54].

Fig 4.1(c) was quite closest in appearance to the reported form of ZrTe_5 powders with experimentally obtained peaks in the given X-Ray diffraction patterns corresponding closely with the standard ICSD database for powder ZrTe_5 (ICSD Code: 085506). The peak at 13° is supposed to have the same relative intensity as the peak at 25° and the crystallite size 97 nm [52], while the peak at 65° is missing. All the other peaks in this XRD corresponded to the orthorhombic phase of ZrTe_5 . This means that XRD peaks corresponding to other phases of ZrTe_5 were not observed.

Fig 4.1(d) is fairly noisy with prominent peaks appearing at 27° , 39° , 40° , 42° , 50° , suggesting that a powder ZrTe_5 phase might be present, even though there could be some peak shift. It is extremely difficult to assess the multiple phases of the sample since it is very noisy background. The crystal size for the most intense peak 27° in this sample is 26 nm.

In figure 4.3, the peaks corresponded quite to the $0k0$ planes of the crystal, that were characteristic for the crystals grown in an a – c plane direction as the maximum exposed surface of the crystal. These peaks can be assigned as (020), (040), (060), (080), and (0100) for 2θ values are 13° , 26° , 38° , 51° , and 65° . The peak at 65° is supposed to have the same

relative intensity as the peak at 65° in the reported work, while the other intensities are the same that could be due to the elemental composition of the sample or preparation conditions.

5.2 X-Ray Photoelectron Spectroscopy

In this study, the successful growth of ZrTe_5 crystal was investigated. In general, Zr has a binding energy range from 190-175 eV and its characteristic peaks are generally observed between 182.7 and 185.5 eV [41], while the binding energy of Te has a range from 587-567, and the characteristic peaks for Te are detected between 573 and 583.7 eV [42], whereas that for the standard calibrating “adventitious carbon” C, is obtained at 285 eV [43]. From XPS data it is evidence to say that all these peaks can be seen in our spectra.

Presented in figure 4.4 is the survey spectra of the sample with $\text{Zr} = 0.0675$ and $\text{Te} = 0.469$ for the binding energy range between 0 – 700 eV and characteristic peaks of Zr, Te, and C can be seen in this spectrum. While the peaks corresponding to O (534 eV), Te (572.3 and 583.7 eV) are quite sharp and intense, the peaks corresponding to C (285 eV) and Zr (183 and 185.5 eV) are low and broad. Whereas, figure 4.5 (a) displays the high-resolution XPS of the Zr 3d. The characteristic $3d_{3/2}$ and $3d_{5/2}$ doublet of the Zr can be seen at 182.7 and 185.2 eV, respectively. These peaks are broad and have low intensities, which could be due to the low concentrations of Zr. Figure 4.5 (b) shows the high-resolution XPS of Te. The characteristic doublet of 3d Te $3d_{3/2}$ and $3d_{5/2}$ exist at 573.2 and 583.5 eV, which confirming the attendance of Te in the specimen. The relatively high intensities of Te is due to the excessive amount of Te in the sample [44].

Displayed in figure 4.6 is the survey spectra of the sample with $\text{Zr} = 0.05$ and $\text{Te} = 0.361$ for the binding energy range between 0 – 700 eV and the characteristic peaks of Te, Zr,

O and C. The peak corresponding to O (536 eV), Te (573 and 583 eV) are quite sharp and intense, while the peaks corresponding to Zr (182.5 and 185 eV) and C (283.7 eV) are low and broad. However, figure 4.7 (a) presents the high-resolution XPS of the Zr 3d. The characteristic $3d_{3/2}$, $3d_{5/2}$ doublet of Zr can be seen at 182.5 and 185.2 eV, respectively. These peaks are broad and have low intensities, probably due to the low concentrations of Zr. However, we note some additional satellite peaks that are not supposed to be there. Figure 4.7 (b) shows the high-resolution XPS of Te and the characteristic doublet of 3d Te, $3d_{3/2}$, and $3d_{5/2}$ exist at 573 and 583.5 eV, respectively, indicating the presence of Te in the sample.

The difference in the intensities can be attributed to the peak processing such as smoothing, that can alter the relative intensity of the peaks. The XPS technique is a surface phenomenon and “whatever data has been extracted is based on the data on the surface” [45]. In other words, XPS can detect extremely small amounts of absorbed O from the material surface. This is why the peaks corresponding to O is clearly visible in the samples. It is easy for environmental oxygen to adsorb on the surface of the crystal [46]. However, the C peak is often referred to “Adventitious Carbon” that supposed to be at 284.5- 285 eV. In addition, the material surface can have hanging or incomplete bonds, which can result in shifting the BE to lower energy values or reduce the intensity of the peaks [47].

Zr 3d 5/2 Peak

The position of the Zr $3d_{5/2}$ peak for the first sample was obtained at 182.5, which is well within the range of the expected position of Zr. For the second samples, the $3d_{5/2}$ peak was obtained at 185.2 eV, which is the same as that as the first powder. In literature, the Zr $3d_{5/2}$ peak of $ZrTe_5$ is reported at about 183 eV [64]. The second sample had an additional peak on the lower BE of the $3d_{5/2}$ peak which may be due to an impurity. Since it has a lower

BE, it could mean there is a mixed phase of Zr, or there could be ZrO_2 . All these are possibilities and are consequences of the methods of synthesis.

Te 3d_{5/2} Peak

The Te 3d_{5/2} is reported between 571 and 576.3. In some specially grown (Pb,Ge)Te composites, the Te 3d_{5/2} peak was obtained at 571.5eV. In a PbTe material, the Te peak was obtained at 572.3 eV and in GeTe, it was observed at 571.8eV [63]. In the XPS of the first and second samples, the Te 3d_{5/2} peaks range between 573 and 573.2 eV, which are well within the reported values of Te [63]. In the case of ZrTe₅, the Te peak has also been reported around 573 eV, suggesting that there is Te present in the sample. However, phase quantification using XPS is almost impossible since this is primarily a surface technique. However, the relative peak intensities and the ratio of the area under the curves for the Zr and Te peaks would give a decent approximation as to the relative atomic ratio between the two elements [64]. It can be seen in all the samples that the counts on the intensity axis is much higher for Te compared to Zr. This shows that the concentration of Te in the samples are much more, confirming that perhaps the Zr:Te ratio is about 1:5.

5.3 Scanning Electron Microscopy Discussion

In this experiment, figure 4.9 displays the first attempt of growing nanosprings on a silica. It can be observed that the ZrTe₅ did not cover uniform nanosprings, and also it can be seen there are some parts did not cover at all, and some parts are very dense, so these make it difficult to distinguish the nanosprings. Hence, these effect on the results, and there are no more nanosprings on the sample. Also, we can notice that, the present of the nanosprings in this sample prevents the growth of ZrTe₅. Figure 4.10 presents the layers of ZrTe₅ at 1.20 k x

magnification with Zr; Te concentrations of 0.05 and 0.36 respectively. We can obviously see the very uniform layers of ZrTe_5 that are stacking on top of each other, and we can also notice some layers are peeling off this probably due to the heat. In figures 4.11, It can be clearly seen the first image shows some layers of the zirconium telluride are peeling off, while another image shows uniform layers. However, in figure 4.12., it is difficult to see the layers, but it has a uniform coating as expected. Finally, figure 4.13 indicates that, some parts are layer by layer and some parts are very dense. So, by comparing this figure with figure 4.12, we can evidently notice how the difference in the concentrations play a role. Hence, when the materials are increased to 1 g, we are able to observe the layers of ZrTe_5

CHAPTER 6: Conclusions

The samples were synthesized through a chemical vapor transport technique and the detailed recipe for the successful synthesis and crystal growth conditions have been elaborately mentioned in this paper. The synthesized materials were characterized using XRD, XPS and SEM. The X-Ray diffraction for sixth and the last attempts present the successful crystals phase of $ZrTe_5$, while the fifth attempt shows some phases for $ZrTe_5$, which is the closest in appearance to the reported form of $ZrTe_5$ powders. The fourth attempt illustrate a powder $ZrTe_5$ phase might be present even it is difficult to assess the phases. Thus, the successful growth of $ZrTe_5$ was achieved after adjusting the growth parameters such as the concentration of the transport agent, the temperature gradients, and the shape of the ampoule. For the XPS measurements of the samples with different Zr:Te ratios, resulted in almost similar results. While for the all the two samples, the Zr 3d doublet peaks were low in intensity and clearly visible, there were a few additional satellite peaks observed for the first sample. However, the Te doublets in all cases were sharp and highly intense, confirming that Te was in excess and the relative intensities of the peaks suggested that Zr:Te composition was almost 1:5. The SEM images for sixth and last attempt illustrate the layers of $ZrTe_5$, and these samples are $ZrTe_5$, while the fourth attempt could be $ZrTe_5$ but the layers are not clearly visible.

References

1. Furuseth, Sigrid, Leif Brattas, and Arne Kjekshus. "Crystal Structure of HfTe 5." *Acta Chemica Scandinavica* 27.7 (1973): 2367-2374.
2. Skelton, E. F., et al. "Giant resistivity and X-ray diffraction anomalies in low-dimensional ZrTe5 and HfTe5." *Solid state communications* 42.1 (1982): 1-3.
3. Jones, T. E., et al. "Thermoelectric power of HfTe5 and ZrTe5." *Solid State Communications* 42.11 (1982): 793-798.
4. Ali, Mazhar N., et al. "Large, non-saturating magnetoresistance in WTe₂" *Nature* 514.7521 (2014): 205-208.
5. Tamai, Anna, et al. "Fermi arcs and their topological character in the candidate type-II Weyl semimetal MoTe 2." *Physical Review X* 6.3 (2016): 031021.
6. Soluyanov, Alexey A. et al. "Type-II Weyl Semimetals." *Nature* 527.7579 (2015): 495-498.
7. Zhu, Ziming, et al. "Triple point topological metals." *Physical Review X* 6.3 (2016): 031003.
8. Takahashi, S., et al. "Transport and elastic anomalies in ZrTe3." *Solid state communications* 49.11 (1984): 1031-1034.
9. Izumi, M., et al. "TRANSPORT PROPERTIES AND FERMI SURFACES IN HfTe5 AND ZrTe5." *Le Journal de Physique Colloques* 44.C3 (1983): C3-1705.

10. Littleton IV, R. T., et al. "Transition-metal pentatellurides as potential low-temperature thermoelectric refrigeration materials." *Physical Review B* 60.19 (1999): 13453.
11. DiSalvo, F. J., R. M. Fleming, and J. V. Waszczak. "Possible phase transition in the quasi-one-dimensional materials ZrTe₅ or HfTe₅." *Physical Review B* 24.6 (1981): 2935.
12. Jaime, M., et al. "Coexistence of localized and itinerant carriers near T_C in calcium-doped manganites." *Physical Review B* 60.2 (1999): 1028.
13. Rubinstein, Mark. "Two-component model of polaronic transport." *Journal of Applied Physics* 87.9 (2000): 5019-5021.
14. Weng, Hongming, Xi Dai, and Zhong Fang. "Transition-metal pentatelluride ZrTe₅ and HfTe₅: A paradigm for large-gap quantum spin Hall insulators." *Physical review X* 4.1 (2014): 011002.
15. Li, Qiang et al. "Chiral Magnetic Effect in ZrTe₅." *Nature Physics* 12.6 (2016): 550-554.
16. Fan, Zongjian et al. "Transition Between Strong and Weak Topological Insulator In ZrTe₅ And HfTe₅." *Scientific Reports* 7 (2017): 45667.
17. Chen, R. Y., et al. "Magnetoinfrared spectroscopy of Landau levels and Zeeman splitting of three-dimensional massless Dirac fermions in ZrTe₅." *Physical review letters* 115.17 (2015): 176404.
18. Wu, R., et al. "Evidence for topological edge states in a large energy gap near the step edges on the surface of ZrTe₅." *Physical Review X* 6.2 (2016): 021017.
19. Zhang, Yan, et al. "Electronic evidence of temperature-induced Lifshitz transition and topological nature in ZrTe₅." *Nature Communications* 8 (2017) 1552.

20. Moreschini, L., et al. "Nature and topology of the low-energy states in ZrTe 5." *Physical Review B* 94.8 (2016): 081101.
21. Qi, Xiao-Liang, and Shou-Cheng Zhang. "Topological insulators and superconductors." *Reviews of Modern Physics* 83.4 (2011): 1057.
22. Hasan, M. Zahid, and Charles L. Kane. "Colloquium: topological insulators." *Reviews of Modern Physics* 82.4 (2010): 3045.
23. Ando, Yoichi. "Topological insulator materials." *Journal of the Physical Society of Japan* 82.10 (2013): 102001.
24. Chen, Y. L., et al. "Experimental realization of a three-dimensional topological insulator, Bi₂Te₃." *Science* 325.5937 (2009): 178-181.
25. Zhang, Haijun, et al. "Topological insulators in Bi₂Se₃, Bi₂Te₃ and Sb₂Te₃ with a single Dirac cone on the surface." *Nature physics* 5.6 (2009): 438.
26. Okada, Shigeto, Takashi Sambongi, and Masayuki Ido. "Giant resistivity anomaly in ZrTe₅." *Journal of the Physical Society of Japan* 49.2 (1980): 839-840.
27. Yao, Yugui, et al. "Spin-orbit gap of graphene: First-principles calculations." *Physical Review B* 75.4 (2007): 041401.
28. Novoselov, Kostya S., et al. "Electric field effect in atomically thin carbon films." *science* 306.5696 (2004): 666-669.
29. Tang, Peizhe, et al. "Weak topological insulators induced by the interlayer coupling: A first-principles study of stacked Bi₂Te₃." *Physical Review B* 89.4 (2014): 041409.

30. Murakami, Shuichi. "Quantum spin Hall effect and enhanced magnetic response by spin-orbit coupling." *Physical Review Letters* 97.23 (2006): 236805.
31. Manzoni, Giulia. "A Comprehensive ARPES Study on the Anomalous Transport Properties and Topological Character of ZrTe₅." Trieste: Giulia Manzoni, 2016.
32. Hirahara, Toru, et al. "Interfacing 2D and 3D topological insulators: Bi (111) bilayer on Bi₂Te₃." *Physical review letters* 107.16 (2011): 166801.
33. Birkholz, Mario. "Principles of X-ray Diffraction." *Thin Film Analysis by X-Ray Scattering* (2006): 1-40.
34. Hull, A. W. "A new method of chemical analysis." *Journal of the American Chemical Society* 41.8 (1919): 1168-1175.
35. Prince, Edward. *International Tables for Crystallography*. 2nd ed. Chichester: J. Wiley & Sons for the International union of crystallography, 2011. Print.
36. Warren, Bertram Eugene. *X-ray Diffraction*. Courier Corporation, 1969.
37. Whittig, L. D., and W. R. Allardice. "X-ray diffraction techniques." *Methods of Soil Analysis: Part 1—Physical and Mineralogical Methods* methodsofsoilan1 (1986): 331-362.
38. S.A, ARL Applied Research Laboratories. "Basics of X-ray Diffraction." *Thermo ARL* (1999): 2-18.
39. Moulder, John F. *Handbook of X-ray photoelectron spectroscopy: a reference book of standard spectra for identification and interpretation of XPS data*. Eds. Jill Chastain, and

- Roger C. King. Eden Prairie, Minnesota: Physical Electronics Division, Perkin-Elmer Corporation, 1992.9.
40. Haerle, Rainer, et al. "sp²/s p³ hybridization ratio in amorphous carbon from C 1 s core-level shifts: X-ray photoelectron spectroscopy and first-principles calculation." *Physical Review B* 65.4 (2001): 045101.
 41. Hollander, Jack M., and William L. Jolly. "X-ray photoelectron spectroscopy." *Accounts of chemical research* 3.6 (1970): 193-200.
 42. Watts, John F. "X-ray photoelectron spectroscopy." *Vacuum* 45.6-7 (1994): 653-671.
 43. SEM: Scanning Electron Microscope 2017.wikipedia.org. Web.
 44. Yang, Dongxing, et al. "Chemical analysis of graphene oxide films after heat and chemical treatments by X-ray photoelectron and Micro-Raman spectroscopy." *Carbon* 47.1 (2009): 145-152. 42.
 45. Chen, J., et al. "X-ray photoelectron spectroscopy study of disordering in Gd₂(Ti_{1-x}Zr_x)₂O₇ pyrochlores." *Physical review letters* 88.10 (2002): 105901. 43.
 46. Zhou, Yonghui, et al. "Pressure-induced superconductivity in a three-dimensional topological material ZrTe₅." *Proceedings of the National Academy of Sciences* 113.11 (2016): 2904-2909.
 47. Whangbo, Myung Hwan, and Pascal Gressier. "Band structure of niobium tetratelluride (NbTe₄)." *Inorganic Chemistry* 23.9 (1984): 1228-1232.
 48. Chusuei, Charles C., and D. Wayne Goodman. "X-ray photoelectron spectroscopy." *Encyclopedia of physical science and technology* 17 (2002): 921-938.

49. Zhou, Jing-Hong, et al. "Characterization of surface oxygen complexes on carbon nanofibers by TPD, XPS and FT-IR." *Carbon* 45.4 (2007): 785-796.
50. Dersch, H., J. Stuke, and J. Beichler. "Light-induced dangling bonds in hydrogenated amorphous silicon." *Applied Physics Letters* 38.6 (1981): 456-458.
51. Lv, Yang-Yang, et al. "Microstructure, growth mechanism and anisotropic resistivity of quasi-one-dimensional ZrTe₅ crystal." *Journal of Crystal Growth* 457 (2017): 250-254.
52. Fjellvåg, H., and A. Kjekshus. "Structural properties of ZrTe₅ and HfTe₅ as seen by powder diffraction." *Solid State Communications* 60.2 (1986): 91-93.
53. Manzoni, Giulia, et al. "Evidence for a Strong Topological Insulator Phase in ZrTe₅." *Physical review letters* 117.23 (2016): 237601.
54. Skelton, E. F., et al. "Giant resistivity and X-ray diffraction anomalies in low-dimensional ZrTe₅ and HfTe₅." *Solid state communications* 42.1 (1982): 1-3.
55. Eaglesham, D. J., J. Mulcahy, and J. A. Wilson. "Structural polytypes of ZrTe₅." *Journal of Physics C: Solid State Physics* 20.3 (1987): 351.
56. Sambongi, T., et al. "Structural modification and heat capacity of ZrTe₅." *Synthetic metals* 10.3 (1985): 161-168.
57. Birkholz, Mario. "Principles of X-Ray Diffraction." *Thin Film Analysis by X-Ray Scattering*. Mario Birkholz. Weinheim: John Wiley & Sons, 2006.
58. Waseda, Yoshio, Eiichiro Matsubara, and Kozo Shinoda. *X-Ray Diffraction Crystallography*. Berlin: Springer Berlin, 2014.

59. Font-Bardia, Mercè, and Xavier Alcobé. *X-Ray Single Crystal and Powder Diffraction: Possibilities and Applications*. Barcelona: Centres Científics i Tecnològics de la Universitat de Barcelona, 2010.
60. Thompson, P., D. E. Cox, and J. B. Hastings. "Rietveld refinement of Debye–Scherrer synchrotron X-ray data from Al₂O₃." *Journal of Applied Crystallography* 20.2 (1987): 7983.
61. Universal Industrial Gases, Inc. *Universal Cryo Gas, LLC* . n.d. 2016
62. Zalnezhad, E. et al. "From Zirconium Nanograins to Zirconia Nanoneedles." *Scientific Reports* 6 (2016): 33282. *PMC*. Web. 23 Feb. 2018.
63. Zhu, Tie-Jun, et al. "Controllable synthesis and shape evolution of PbTe three-dimensional hierarchical superstructures via an alkaline method." *The Journal of Physical Chemistry C* 113.19 (2009): 8085-8091. hydrothermal.
64. Qiu, Gang, et al. "Observation of optical and electrical in-plane anisotropy in high-mobility few-layer ZrTe₅." *Nano letters* 16.12 (2016): 7364-7369.
65. Qi, Yanpeng, et al. "Pressure-driven superconductivity in the transition-metal pentatelluride HfTe₅." *Physical Review B* 94.5 (2016): 054517.

APPENDIX 1**Chemical properties of zirconium (Zr)**

Atomic number	40
Atomic mass	91.22 g.mol⁻¹
Electronegativity according to Pauling	1.2
Density	6.49 g.cm⁻³ at 20°C
Melting point	1852 °C
Boiling point	4400 °C
Vanderwaals radius	0.160 nm
Ionic radius	0.08 nm (+4)
Isotopes	11
Electronic shell	[Kr] 4d² 5s²
Energy of first ionisation	669 kJ.mol⁻¹
Energy of second ionisation	1346 kJ.mol⁻¹
Energy of third ionisation	2312 kJ.mol⁻¹
Energy of fourth ionisation	3256 kJ.mol⁻¹

APPENDIX 2

Chemical properties of tellurium (Te)

Atomic number	52
Atomic mass	127.6 g.mol⁻¹
Electronegativity according to Pauling	2.1
Density	6.24 g.cm⁻³
Melting point	450 °C
Boiling point	988 °C
Vanderwaals radius	0.137 nm
Ionic radius	0.221 nm (-2) ; 0.089 nm (+4)
Isotopes	23
Electronic shell	[Kr] 4d¹⁰ 5s²5p⁴
Energy of first ionisation	869.0 kJ.mol⁻¹
Standard potential	- 0.91 V (Sb³⁺/ Sb)
Discovered by	Franz Muller von Reichenstein in 1782

APPENDIX 3

Technical data for Zirconium

Click any property name to see plots of that property for all the elements.

Overview

Name Zirconium
 Symbol Zr
 Atomic Number 40
 Atomic Weight 91.224
 Density 6.511 g/cm³
 Melting Point 1855 °C
 Boiling Point 4409 °C

Thermal properties

Phase Solid
 Melting Point 1855 °C
 Boiling Point 4409 °C
 Absolute Melting Point 2128 K
 Absolute Boiling Point 4682 K
 Critical Pressure N/A
 Critical Temperature N/A
 Heat of Fusion 21 kJ/mol
 Heat of Vaporization 580 kJ/mol
 Specific Heat 278 J/(kg K)^[note]

Classifications

Alternate Names None
 Names of Allotropes None
 Block d
 Group 4
 Period 5
 Series Transition Metal
 Electron Configuration [Kr]5s²4d²
 Color Silver
 Discovery 1789 in Germany
 Gas phase N/A
 CAS Number CAS7440-67-7
 CID Number CID23995
 RTECS Number N/A

Electrical properties

Electrical Type Conductor
 Electrical Conductivity 2.4×10⁶ S/m
 Resistivity 4.2×10⁻⁷ m Ω
 Superconducting Point 0.61

APPENDIX 4

Technical data for Tellurium

Click any property name to see plots of that property for all the elements.

Overview

Name Tellurium
 Symbol Te
 Atomic Number 52
 Atomic Weight 127.6
 Density 6.24 g/cm³
 Melting Point 449.51 °C
 Boiling Point 988 °C

Thermal properties

Phase Solid
 Melting Point 449.51 °C
 Boiling Point 988 °C
 Absolute Melting Point 722.66 K
 Absolute Boiling Point 1261 K
 Critical Pressure N/A
 Critical Temperature N/A
 Heat of Fusion 17.5 kJ/mol
 Heat of Vaporization 48 kJ/mol
 Specific Heat 201 J/(kg K)^[note]

Classifications

Alternate Names None
 Names of Allotropes None
 Block p
 Group 16
 Period 5
 Series Chalcogen
 Electron Configuration [Kr]5s²4d¹⁰5p⁴
 Color Silver
 Discovery 1783 in Romania
 Gas phase N/A
 CAS Number CAS13494-80-9
 CID Number CID6327182
 RTECS Number RTECSWY2625000

Electrical properties

Electrical Type Semiconductor
 Electrical Conductivity 10000 S/m
 Resistivity 0.0001 m Ω
 Superconducting Point N/A